ACS APPLIED OPTICAL MATERIALS



pubs.acs.org/acsaom
Article

# Tuning Electroluminescence from Functionalized SWCNT Networks Further into the Near-Infrared

Nicolas F. Zorn, Simon Settele, Finn L. Sebastian, Sebastian Lindenthal, and Jana Zaumseil*

Cite This: ACS Appl. Opt. Mater. 2023, 1, 1706−1714
Read Online



**ABSTRACT:** Near-infrared electroluminescence from carbon-based emitters, especially in the second biological window (NIR-II) or at telecommunication wavelengths, is difficult to achieve. Single-walled carbon nanotubes (SWCNTs) have been proposed as a possible solution due to their tunable and narrowband emission in the near-infrared region and high charge carrier mobilities. Furthermore, the covalent functionalization of SWCNTs with a controlled number of luminescent $sp^3$ defects leads to even more red-shifted photoluminescence with enhanced quantum yields. Here, we demonstrate that by tailoring the binding configuration of the introduced $sp^3$ defects and hence tuning their optical trap depth, we can generate emission from polymer-sorted (6,5) and (7,5) nanotubes that is mainly located in the telecommunication O-band (1260−1360 nm). Networks of these functionalized nanotubes are integrated in ambipolar, light-emitting field-effect transistors to yield the corresponding narrowband near-infrared electroluminescence. Further investigation of the current- and carrier density-dependent electro- and photoluminescence spectra enables insights into the impact of different $sp^3$ defects on charge transport in networks of functionalized SWCNTs.

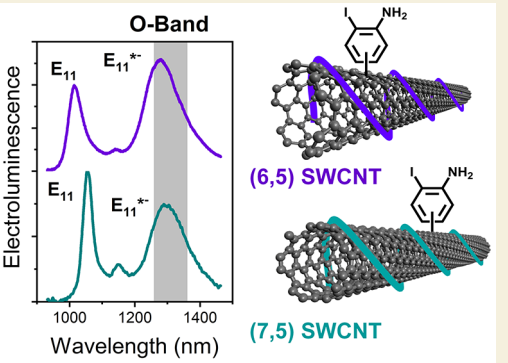


**KEYWORDS:** *telecommunication band, $sp^3$ defects, organic color centers, ambipolar transistors, trap states*

## INTRODUCTION

The near-infrared wavelength range is highly interesting for applications in biological imaging (first and second biological window, NIR-I and NIR-II)[1,2] as well as telecommunication (O-band at 1260−1360 nm and C-band at 1550 nm). For many of the corresponding light-emitting devices, it would be advantageous to move away from conventional inorganic semiconductors and toward solution-processable and flexible materials. However, in stark contrast to the visible range, narrowband near-infrared electroluminescence beyond 800 nm is very difficult to achieve with organic emitters, and even more so beyond 1000 nm. While a number of organic semiconductors with small bandgaps exist (e.g., donor−acceptor polymers[3]) that even show high charge carrier mobilities, they all suffer from very low (below 1%) photoluminescence quantum yields (PLQY),[4−6] often rationalized with the gap law.[7] Consequently, very few examples of near-infrared organic light-emitting diodes or light-emitting transistors have been demonstrated at all. More efficient near-infrared emitters always contain heavier elements such as inorganic quantum dots ($Ag_2S$ and InAs)[8,9] or rare-earth complexes.[10]

Semiconducting single-walled carbon nanotubes (SWCNTs) are a potential alternative as they combine solution-processability, very high hole and electron mobilities, and narrowband emission in the near-infrared, which can be tuned from 900 to over 1600 nm depending on the diameter and (n,m) species (i.e., chirality) of the nanotubes.[11] Several methods for the separation of single nanotube species have been developed and optimized over the past decade to obtain large amounts of pure material.[12] Thus, it is now possible to create optoelectronic devices, including photovoltaic cells,[12] electrochromic cells,[13] light-emitting diodes,[14] and light-emitting transistors[15,16] based on dense networks of a single (n,m) type of nanotubes with narrow and well-controlled absorption and emission bands. However, the more abundant and easiest to purify nanotube species are those with emission bands in the range of 950−1100 nm, such as the (6,5) and (7,5) nanotubes.

Unfortunately, the PLQY of SWCNTs in the near-infrared still only reaches a few percent in dispersion[17] and is even lower in dense networks. In addition to the gap law, dark states, and Auger-quenching by charge carriers,[18] the fast diffusion of excitons within nanotubes toward potential quenching sites (e.g., the ends of the nanotubes)[19] is assumed to be the main cause for the observed low emission efficiencies.

Received: July 31, 2023
Revised: September 8, 2023
Accepted: September 25, 2023
Published: October 16, 2023

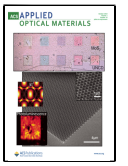

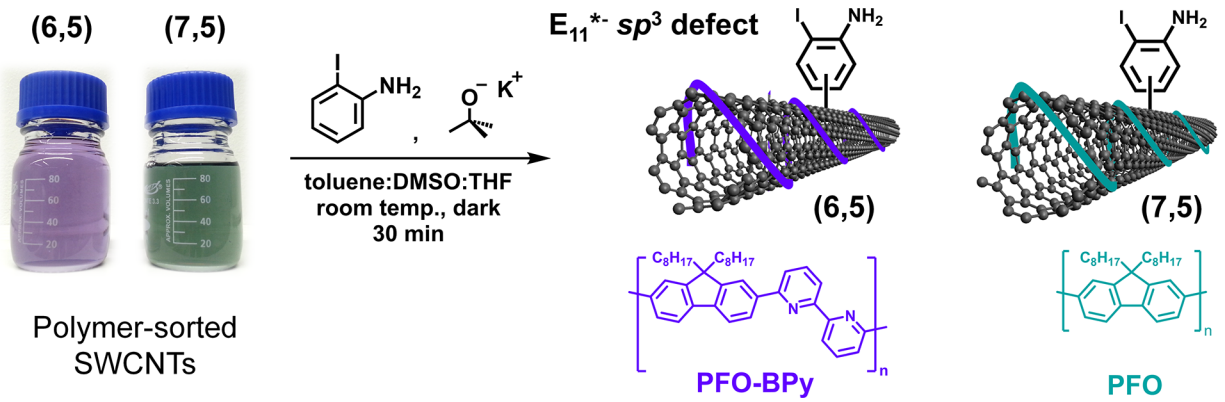


**Figure 1.** General reaction scheme for the covalent functionalization of PFO-BPy-wrapped (6,5) and PFO-wrapped (7,5) SWCNTs with 2-iodoaniline and potassium *tert*-butoxide (KO*t*Bu) in organic solvents to introduce $E_{11}^{*-}$ defects. Note that bond formation between the defect moiety and the SWCNT might occur at different carbon atoms of the aromatic ring.

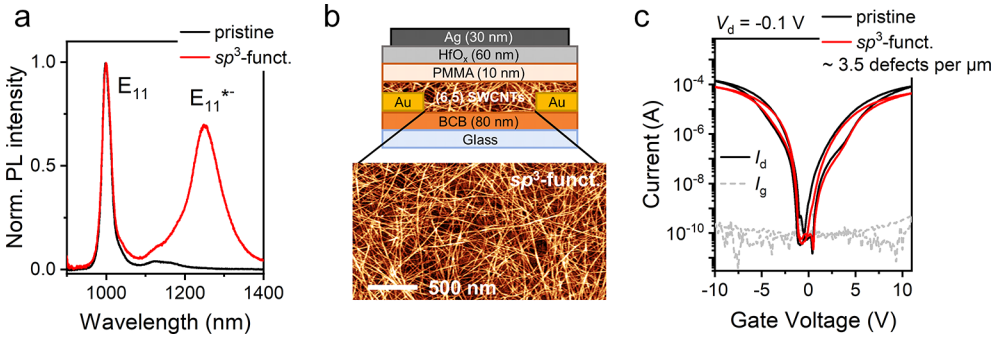


**Figure 2.** (a) Normalized PL spectra of a (6,5) SWCNT dispersion before and after functionalization. Emission peaks corresponding to mobile $E_{11}$ excitons and defect-localized $E_{11}^{*-}$ excitons are labeled. (b) Schematic cross-section of a bottom-contact, top-gate (6,5) SWCNT network FET (layer thicknesses not to scale) and a representative atomic force micrograph of a dense network of $sp^3$-functionalized SWCNTs. The scale bar is 500 nm. (c) Ambipolar transfer characteristics of pristine and functionalized SWCNT network FETs in the linear regime ($V_d = -0.1$ V). Solid lines represent drain currents $I_d$, and gray dashed lines represent gate leakage currents $I_g$.

The controlled introduction of luminescent $sp^3$ defects in SWCNTs[20,21] has been shown to be an effective path to reduce undesired quenching, increase PLQY, and shift the emission wavelength even further into the near-infrared. A small number of specific lattice defects along the nanotube create exciton trap states, where previously mobile excitons are localized. They subsequently decay radiatively from the defect state at longer wavelengths than the mobile excitons (optical trap depths of 150−250 meV).[22] Due to this efficient localization, the excitons are unable to reach other nonradiative defects, and hence the overall PLQY is increased, especially for very short nanotubes.[23]

Several different functionalization methods to create luminescent defects have been developed over the past decade that can be applied to either surfactant-stabilized nanotubes in water[21,24] or polymer-wrapped nanotubes in organic solvents.[13,25] Depending on the employed chemistry, different types of lattice defects are introduced that result in more or less red-shifted emission peaks. Here we will refer to the commonly observed defect emission with optical trap depths of 160−190 meV as the $E_{11}^*$ emission and to the further red-shifted emission as $E_{11}^{*-}$ (optical trap depths > 200 meV).[26] Most studies on $sp^3$ defects in SWCNTs are carried out on (6,5) nanotubes (diameter = 0.76 nm, optical bandgap ≈ 1.27 eV) due to their excellent availability as pure dispersions and their high reactivity to form $sp^3$ defects. Maximum PLQYs of up to 4−5% are typically reached in dispersions of polymer-wrapped (6,5) SWCNTs with 5−8 defects per micrometer.[25,27,28] However, for further red-shifted emission, SWCNTs with larger diameters are preferred, such as (7,5), (9,4), or (10,5) nanotubes. These have also been functionalized and in some cases even showed single-photon emission up to the C-band range at room temperature.[29,30]

The integration of $sp^3$-functionalized SWCNTs in lateral light-emitting diodes and ambipolar field-effect transistors showing electroluminescence (EL) from defects has recently been demonstrated for individual nanotubes[31] as well as sparse[32] and dense networks.[33] The defect emission properties were maintained in these devices, and charge transport was only slightly affected. However, those examples only involved SWCNTs with $E_{11}^*$ defects and did not reach far into the near-infrared. Here we tailor the covalent functionalization of polymer-sorted (6,5) and (7,5) nanotubes to obtain $E_{11}^{*-}$ defect electroluminescence further in the near-infrared using light-emitting transistors with dense SWCNT networks. Emission in the telecommunication O-band is achieved without sacrificing the ambipolar charge transport properties required for high current densities. We further explore the correlation of the optical trap depth and charge carrier trapping for both nanotube species and the carrier-density-dependent photoluminescence and electroluminescence spectra for additional device tunability.


https://doi.org/10.1021/acsaom.3c00261
ACS Appl. Opt. Mater. 2023, 1, 1706−1714

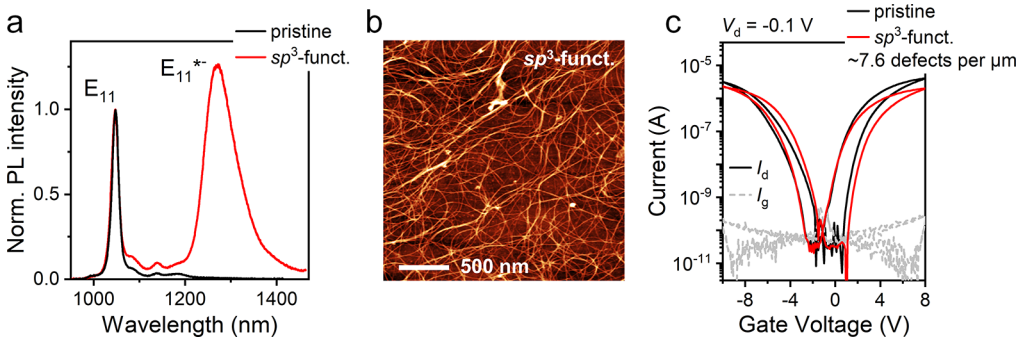


**Figure 3.** (a) Normalized PL spectra of a pristine (7,5) SWCNT dispersion and a dispersion after functionalization. Emission peaks corresponding to mobile $E_{11}$ excitons and defect-localized $E_{11}^{*-}$ excitons are labeled. (b) Representative atomic force micrograph of an aerosol-jet-printed network of $sp^3$-functionalized (7,5) SWCNTs with $E_{11}^{*-}$ defects. The scale bar is 500 nm. (c) Ambipolar transfer characteristics of pristine and functionalized (7,5) SWCNT network FETs in the linear regime ($V_d$ = −0.1 V). Solid lines represent drain currents $I_d$, and gray dashed lines represent gate leakage currents $I_g$.

## RESULTS AND DISCUSSION

To achieve further red-shifted photo- and electroluminescence from networks of polymer-wrapped (6,5) and (7,5) nanotubes, they were first selectively dispersed in toluene by shear-force mixing with PFO-BPy and PFO (see molecular structures in Figure 1), respectively, followed by centrifugation. Subsequently, they were functionalized with $E_{11}^{*-}$ defects using the established reaction with 2-iodoaniline in the presence of potassium *tert*-butoxide (KO*t*Bu, see schematic in Figure 1 and Experimental Section for a detailed description).[25] A portion of the pristine nanotubes was retained for reference in both cases.

The successful introduction of $E_{11}^{*-}$ defects was confirmed by photoluminescence (PL) spectroscopy of the dispersions. Figure 2a shows the PL spectra of pristine and functionalized (6,5) SWCNTs in toluene normalized to the $E_{11}$ emission from mobile excitons at 1000 nm. Only one strongly red-shifted emission peak at 1251 nm resulting from $E_{11}^{*-}$ defects (optical trap depth 248 meV) is evident, and no or only negligible emission from $E_{11}^{*}$ defects (expected at ∼1170 nm) is observed. The amplitude averaged fluorescence lifetime of this defect emission was determined by time-correlated single photon counting (TCSPC) to be 362 ps, which is consistent with the deeper optical trap depth of $E_{11}^{*-}$ compared to $E_{11}^{*}$ defects. Likewise, a functionalized dispersion of (7,5) SWCNTs (see Figure 3a) exhibits an $E_{11}^{*-}$ defect emission peak at 1272 nm compared to the corresponding $E_{11}$ peak at 1048 nm. The optical trap depth for this defect in (7,5) nanotubes, however, is only 208 meV. A reduction of the optical trap depth with increasing nanotube diameter is a common observation for functionalized SWCNTs and was reported for this type of defect as well.[21,25,34] For both functionalized (6,5) and (7,5) nanotubes, the defect emission is close to or already within the O-band for telecommunication (1260−1360 nm). The corresponding absorption and Raman spectra before and after functionalization are shown in Figures S1 and S2.

Pristine and functionalized dispersions were used to create bottom-contact, top-gate field-effect transistors (FETs) with a bilayer gate dielectric of PMMA and $HfO_x$, as introduced previously[33] and schematically shown in Figure 2b. An additional surface passivation layer of BCB (a cross-linked benzocyclobutene-based polymer, see Experimental Section) on the glass substrate prevented undesired sideband emission and enabled nearly intrinsic PL and EL spectra.[35] The SWCNT network density (see inset in Figure 2b and Figure 3b) for all samples was chosen to be well above the percolation limit and above the mobility saturation for nanotube networks[36] to ensure comparability of the extracted mobility values. The obtained transfer characteristics of representative FETs in the linear regime (drain voltage $V_d$ = −0.1 V) are shown in Figures 2c and 3c for the (6,5) and (7,5) SWCNT networks, respectively. All of them exhibit typical ambipolar charge transport with only little hysteresis and high on/off current ratios. The average values of the extracted hole and electron mobilities are summarized in Table S1 with the corresponding defect densities (3.5 and 7.6 $\mu m^{-1}$, respectively) that were determined based on the differential increase of the integrated Raman D/$G^+$ mode ratios, as reported previously.[27] Note that the hole and electron mobilities of the (7,5) networks (∼0.14 $cm^2\ V^{-1}\ s^{-1}$) are much lower than those of the (6,5) nanotubes (∼2−4 $cm^2\ V^{-1}\ s^{-1}$), which is likely due to stronger bundling, as is visible in Figure 3b (average bundle thickness 5−8 nm versus 3−4 nm for (6,5) SWCNTs), and the presence of residual (7,6) nanotubes (see Figure S2) with a smaller bandgap that may act as trap sites.[37] The increased bundling of (7,5) nanotubes and hence the less efficient removal of adsorbed water from the network at moderate annealing temperatures may also explain the larger hysteresis for electron transport in these transistors (Figure 3c).

Importantly, the reduction of the hole (from 3.9 to 2.2 $cm^2\ V^{-1}\ s^{-1}$) and electron mobilities (from 2.1 to 1.1 $cm^2\ V^{-1}\ s^{-1}$) for the (6,5) nanotube networks at a relatively low defect density indicates a similar if not stronger impact of the $E_{11}^{*-}$ defects on charge transport within the nanotubes compared to the previously investigated $E_{11}^{*}$ defects.[33,38] The (7,5) nanotube networks show a similar behavior, with a reduction of the mobility by half for slightly higher defect densities. The substantially deeper optical trap depth of the $E_{11}^{*-}$ defects in the (6,5) SWCNTs (268 meV) compared to both the $E_{11}^{*}$ (160−190 meV) and $E_{11}^{*-}$ defects in the (7,5) nanotubes (208 meV) may also reflect the trap depth for charge carriers and hence rationalize the stronger impact on charge carrier mobilities.

Further insights into the possible trapping of charge carriers by $sp^3$ defects can be gained from in situ PL spectroscopy of the nanotube networks when electrostatically doped in FETs. For that, only a very small drain bias was applied (−0.01 V) to ensure a nearly uniform distribution of charges within the channel while still being able to record transfer characteristics. The gate voltage was increased stepwise to control the induced


https://doi.org/10.1021/acsaom.3c00261
ACS Appl. Opt. Mater. 2023, 1, 1706−1714

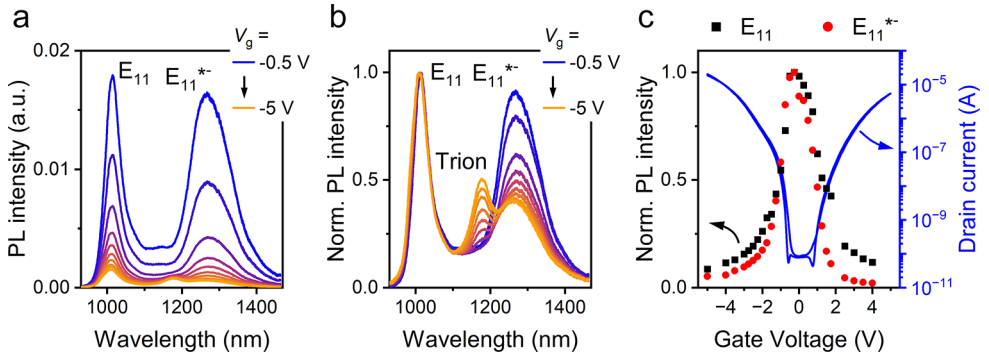


**Figure 4.** (a) Absolute and (b) normalized PL spectra (nonresonant excitation at 785 nm) of a (6,5) SWCNT network FET with $E_{11}^{*-}$ defects at different gate voltages $V_g$ in hole accumulation ($V_d$ = −0.01 V). At higher $V_g$ values, the trion emission becomes visible in the normalized spectra. (c) PL intensities of $E_{11}$ (black squares) and $E_{11}^{*-}$ (red circles) versus $V_g$ obtained from peak fits and normalized to their maxima. A corresponding transfer curve (linear regime, $V_d$ = −0.1 V) is shown in blue (right axis).

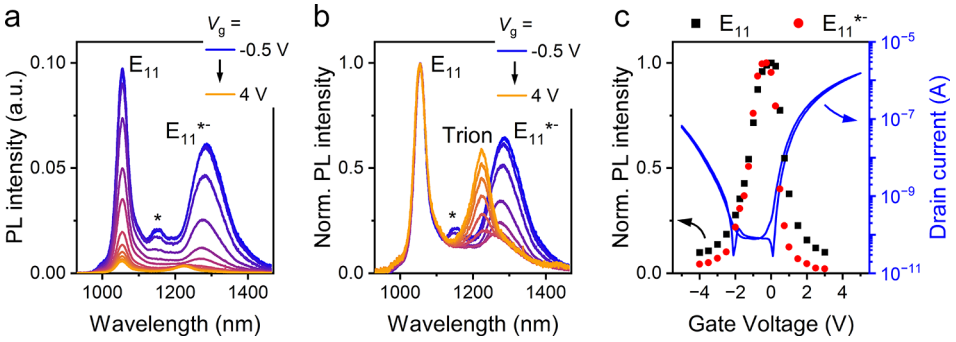


**Figure 5.** (a) Absolute and (b) normalized PL spectra (nonresonant excitation at 785 nm) of a (7,5) SWCNT network FET with $E_{11}^{*-}$ defects at different gate voltages $V_g$ in electron accumulation ($V_d$ = −0.01 V). At high voltages, the trion emission becomes visible in the normalized spectra. The asterisk marks the $E_{11}$ emission peak of residual (7,6) SWCNTs. (c) PL intensities of $E_{11}$ (black squares) and $E_{11}^{*-}$ (red circles) versus $V_g$ obtained from peak fits and normalized to their maxima and corresponding transfer curve (linear regime, $V_d$ = −0.1 V) in blue (right axis).

charge carrier density (holes or electrons). The nanotube network in the middle of the channel was excited with a 785 nm laser diode, and PL spectra were recorded using an InGaAs line camera (see Experimental Section). Charge carriers in semiconducting SWCNTs lead to efficient PL quenching through Auger recombination as well as the formation of trions (charged excitons).[39−41] The overall reduced emission intensity from functionalized (6,5) nanotube networks with increasing concentrations of holes (for negative applied gate voltages) is shown in Figure 4a. However, the normalized spectra (Figure 4b) clearly show stronger quenching of $E_{11}^{*-}$ defect emission compared to $E_{11}$ for the same carrier densities (i.e., gate voltages) as well as the emergence of trion emission at 1178 nm. Note that for in situ PL measurements of (6,5) nanotubes with $E_{11}^{*}$ defects, the trion and defect emission peaks overlap, thus making an independent analysis difficult.[33] The data here also clearly show that trion and defect emissions have different origins and are not related.

When plotting the normalized PL intensities of the $E_{11}^{*-}$ and $E_{11}$ emissions (resolved by fitting as Gaussian peaks) versus the applied gate voltage (Figure 4c), a small voltage offset in the drop of the PL intensity for both hole and electron accumulation becomes apparent. As was introduced by Tanaka et al. for spectro-electrochemical measurements of pristine nanotubes[42] and later applied to functionalized SWCNTs,[43,44] fitting the PL intensity versus the gate voltage to a Nernst-type equation enables the extraction of the voltage differences ($\Delta V_{g,1/2}$) between hole and electron accumulation that can be associated with the effective bandgap. For the $E_{11}$ emission, $\Delta V_{g,1/2}$ was determined to be 2.87 V versus 2.17 V for $E_{11}^{*-}$ (see Figure S3 and Table S2), suggesting a narrower effective bandgap around the defect. Very similar PL quenching behavior was observed for functionalized (7,5) nanotubes, as shown in Figure 5. The corresponding voltage differences $\Delta V_{g,1/2}$ were 2.42 V for quenching of the $E_{11}$ emission and 1.86 V for $E_{11}^{*-}$ (see Figure S4 and Table S2). As expected, the difference between the $\Delta V_{g,1/2}$ values for $E_{11}$ of the (6,5) and (7,5) SWCNTs correlates with their electronic bandgaps (1.27 and 1.21 eV, respectively) but is not a quantitative value. The smaller offset between the $\Delta V_{g,1/2}$ values for $E_{11}$ and $E_{11}^{*-}$ of (6,5) and (7,5) SWCNTs (0.7 versus 0.56 V) also scales roughly with the difference in the optical trap depths (268 versus 208 meV). These measurements suggest that $E_{11}^{*-}$ defects not only localize excitons but are also directly related to changes in the local valence and conduction band energies in comparison to the surrounding pristine nanotube and can thus act as shallow traps for both holes and electrons. Given the nearly identical reductions in hole and electron mobility, it is reasonable to assume that the charge trap depths are very similar, although electron-withdrawing or -pushing substituents may have an additional impact.[44,45]

The gate-voltage-dependent PL quenching indicated that charges could be trapped at the defect sites. To obtain more detailed information about the interaction of charge carriers with $E_{11}^{*-}$ defects and defect-localized excitons, PL lifetime measurements by TCSPC were performed on electrostatically doped (gated) nanotube networks. Note that an analysis of the very short lifetime of the $E_{11}$ emission (i.e., mobile excitons) in


https://doi.org/10.1021/acsaom.3c00261
ACS Appl. Opt. Mater. 2023, 1, 1706−1714

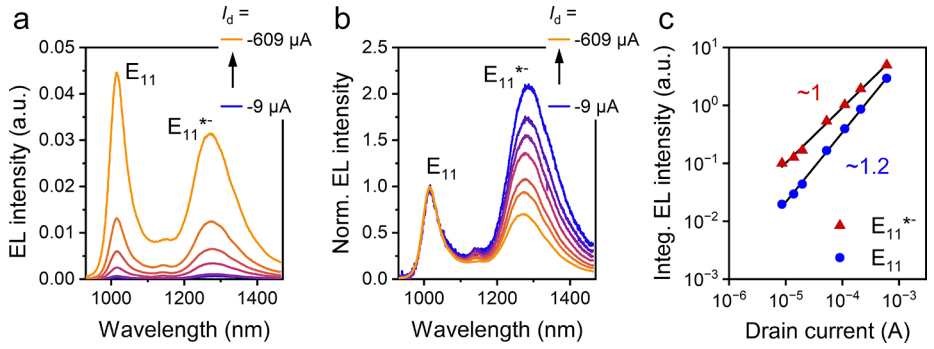


**Figure 6.** (a) Absolute and (b) normalized EL spectra of a (6,5) SWCNT network light-emitting FETs with $E_{11}^{*-}$ defects in the ambipolar regime for different drain currents $I_d$. (c) Double-logarithmic plot of the integrated EL intensities versus $I_d$. Blue circles correspond to $E_{11}$ emission, and red triangles correspond to $E_{11}^{*-}$ defect emission (integration from 950−1100 and 1150−1450 nm, respectively). Black solid lines are linear fits to the data, numbers indicate the corresponding slopes.

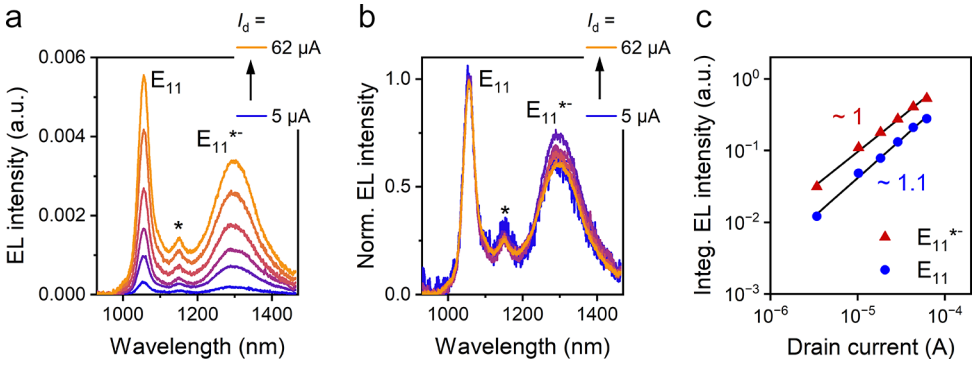


**Figure 7.** (a) Absolute and (b) normalized EL spectra of a (7,5) SWCNT network light-emitting FET with $E_{11}^{*-}$ defects in the ambipolar regime for different drain currents $I_d$. The asterisk marks the $E_{11}$ peak of residual (7,6) SWCNTs. (c) Double-logarithmic plot of the integrated EL intensities versus $I_d$. Blue circles correspond to $E_{11}$ emission, and red triangles correspond to $E_{11}^{*-}$ defect emission (integration from 950−1120 and 1190−1450 nm, respectively). Black solid lines are linear fits to the data, numbers indicate the corresponding slopes.

the SWCNT networks (<10 ps) was not possible due to limitations by the instrument response function (IRF) of the employed setup. However, in the undoped state, PL traces of the $E_{11}^{*-}$ emission could be fitted with a biexponential decay with a short (83 ps) and long (281 ps) lifetime component (see Figure S5), as commonly observed for $sp^3$ defects at room temperature.[46] The short lifetime might be assigned to the redistribution of the exciton population over the defect-state manifold, whereas the long lifetime encompasses all radiative and nonradiative decay pathways of defect-localized excitons.[47] Both lifetimes progressively decrease (to 32 and 129 ps, respectively) with increasing carrier density (here only shown for hole accumulation). These trends are in good agreement with charge-induced Auger-quenching as a very fast and efficient nonradiative decay path for defect-localized excitons. The PL lifetime data further corroborate the notion that charge carriers are indeed trapped at $E_{11}^{*-}$ defect sites, leading to more nonradiative exciton decay as well as lower carrier mobilities.

Finally, EL from the (6,5) and (7,5) nanotubes with $E_{11}^{*-}$ defects was explored. Despite the indicated charge trapping at defects, the SWCNT networks still showed balanced hole and electron transport even at reasonably high defect densities (see above), which is required for light-emitting FETs. The respective FETs were operated in the ambipolar regime at high drain voltages to accumulate both holes and electrons in the channel and create a recombination and emission zone as described in detail elsewhere.[48] The applied voltages were chosen such that the emission zone (width 1−2 $\mu$m) was located in the middle of the channel (channel length 40 $\mu$m) to avoid any potential effects of carrier imbalance, contact resistance, or the edge of the metal electrodes. The overall drain current (proportional to the number of hole-electron recombination events) was varied by adjusting the voltages and was kept constant throughout the collection of EL spectra. Figure 6a shows the obtained EL spectra from functionalized (6,5) SWCNTs with clear $E_{11}$ emission at ∼1015 nm as well as emission from the $E_{11}^{*-}$ defects at ∼1280 nm. Importantly, the maximum of the defect emission peak was located well within the telecommunication O-band (1260−1360 nm), and at low drain currents, more than 85% of photons were emitted through this defect channel. The overall external quantum efficiency for these devices was estimated to be 0.015% and thus similar to previous light-emitting FETs with functionalized SWCNTs.[33]

As the drain current was increased, the integrated EL intensity also increased, as shown for light-emitting FETs with functionalized (6,5) SWCNTs (Figure 6a) and for pristine (6,5) nanotubes (Figure S6). Normalization of the spectra to the $E_{11}$ emission peak (Figure 6b) demonstrates that $E_{11}^{*-}$ defect emission dominates at low current densities but saturates compared to the $E_{11}$ emission at higher current densities. This trend is also reflected in the double logarithmic plot of integrated EL peak intensities versus drain currents (Figure 6c). The slope for defect emission is slightly lower than for mobile exciton emission, although both are close to unity


https://doi.org/10.1021/acsaom.3c00261
ACS Appl. Opt. Mater. 2023, 1, 1706−1714

and hence are close to a linear increase of emission with current density.

These different dependencies are not due to trapping of excitons at the defect sites and subsequent state filling, as is observed for the pulsed excitation of functionalized nanotubes at high excitation power.[25,28] The estimated exciton density at the given current densities is still too low to be responsible for this effect. It is more likely that the trapping of holes and electrons at the defects leads to more efficient Auger quenching of defect emission at higher carrier densities, similar to the stronger PL quenching discussed above. Note that such strong current density dependence of defect emission was not observed for the $E_{11}^*$ defect emission of (6,5) SWCNTs,[33] probably due to the lower trap depth (160−190 meV) compared to $E_{11}^{*-}$ defects (268 meV).

The EL spectra from ambipolar light-emitting FETs based on functionalized (7,5) nanotubes are shown in Figure 7a. In addition to the emission peaks from mobile excitons in (7,5) nanotubes at 1055 nm and residual (7,6) SWCNTs at 1150 nm, a significant number of photons originate from the $E_{11}^{*-}$ defects, with emission centered around 1300 nm and thus fully within the O-band for telecommunication. The EL spectra of pristine (7,5) nanotubes only show $E_{11}$ emission from mobile excitons as well as some trion emission (∼1225 nm) at higher current densities (see Figure S7). The ratio of $E_{11}$ to $E_{11}^{*-}$ emission from light-emitting FETs with functionalized (7,5) SWCNTs (see normalized EL spectra in Figure 7b and double logarithmic plots in Figure 7c) does not change, and the overall intensity increases roughly linearly with the current. The reduced current density dependence of the $E_{11}^{*-}$ emission might be due to the limited drain current range (due to the lower carrier mobilities) and the lower trap depth compared to FETs with functionalized (6,5) nanotubes. Note that the low drain currents also prevented a reliable determination of external quantum efficiencies for EL from pristine or functionalized (7,5) nanotubes.

## CONCLUSIONS

In summary, we have demonstrated near-infrared electroluminescence in the telecommunication O-band from dense networks of $sp^3$-functionalized (6,5) and (7,5) single-walled carbon nanotubes in light-emitting FETs. The majority of photons are emitted from the luminescent defects at 1280−1300 nm, and emission intensities scale roughly linearly with current density. The controlled introduction of $E_{11}^{*-}$ defects with further red-shifted emission provides direct access to emission wavelengths beyond 1200 nm, even with small-diameter nanotubes, which are easily purified and functionalized in large amounts. Furthermore, the investigated ambipolar light-emitting field-effect transistors gave insights into the impact of the specific luminescent defects and their optical trap depth on the local valence and conduction band energies around the defect site. Their charge trapping properties depend on both their binding configuration ($E_{11}^*$ or $E_{11}^{*-}$) and the diameter of the nanotube. The presented data showcase the spectral tunability of $sp^3$ defect emission, as achieved by choice of the SWCNT species and control over the defect binding configuration through functionalization chemistry while retaining good charge transport. This combination should enable the application of covalently functionalized SWCNTs in near-infrared light-emitting devices, although improvements of the emission efficiency will be required.

## EXPERIMENTAL SECTION

### Preparation of (6,5) and (7,5) SWCNT Dispersions

Highly purified (6,5) and (7,5) SWCNT dispersions in toluene were obtained from CoMoCAT raw material (Sigma-Aldrich, batch MKCJ7287, 0.4 g $L^{-1}$) via selective polymer-wrapping under shear force mixing (Silverson L2/Air mixer, 10 230 rpm, 72 h, 20 °C), as described previously.[17] The (6,5) SWCNTs were extracted with the fluorene-bipyridine copolymer poly[(9,9-dioctylfluorenyl-2,7-diyl)-*alt*-(6,6′-(2,2′-bipyridine))] (PFO-BPy, American Dye Source, $M_W$ = 40 kg $mol^{-1}$, 0.5 g $L^{-1}$), whereas the (7,5) SWCNTs were selectively dispersed with poly(9,9-dioctylfluorene) (PFO, Sigma-Aldrich, $M_W$ > 20 kg $mol^{-1}$, 0.9 g $L^{-1}$). The resulting dispersions after shear force mixing were centrifuged twice for 45 min at 60 000 *g* (Beckman Coulter Avanti J26XP centrifuge), and the combined supernatants were filtered through a poly(tetrafluoroethylene) (PTFE) syringe filter (pore size 5 μm) to remove the larger aggregates.

### Covalent Functionalization of Polymer-Wrapped (6,5) and (7,5) SWCNTs

Luminescent $E_{11}^{*-}$ defects were introduced to polymer-wrapped (6,5) and (7,5) SWCNTs according to the protocol developed by Settele et al.[25] To reduce the content of unbound wrapping polymer prior to the functionalization reaction, the dispersions obtained by shear force mixing were filtered through a PTFE membrane filter (Merck Millipore JVWP, 0.1 μm pore size), washed with toluene (10 mL), and redispersed in fresh toluene by bath sonication. SWCNTs were functionalized with 2-iodoaniline (Sigma-Aldrich, 98%) in the presence of the strong organic base potassium *tert*-butoxide (KO*t*Bu, Sigma-Aldrich, 98%). First, the aniline compound was dissolved in toluene, and dimethyl sulfoxide (DMSO, Sigma-Aldrich, anhydrous) and a solution of KO*t*Bu in tetrahydrofuran (THF, Sigma-Aldrich, anhydrous) were added to the solution. Then, the polymer-depleted SWCNT dispersion in toluene was added to the reaction mixture so that the optical density at the $E_{11}$ absorption peak was 0.3 $cm^{-1}$ (concentrations of 0.54 μg $mL^{-1}$ for the (6,5) SWCNTs and 0.86 μg $mL^{-1}$ for the (7,5) SWCNTs). The concentrations of the aniline compound and KO*t*Bu in the final reaction mixture were 29.3 and 58.6 mmol $L^{-1}$, respectively, and the volumetric fractions were 83.3:8.3:8.3 toluene:DMSO:THF. The reaction proceeded under stirring and in the dark over 30−180 min before it was terminated by vacuum filtration through a PTFE membrane filter (Merck Millipore JVWP, 0.1 μm pore size). The collected nanotubes were thoroughly washed with methanol and toluene (10 mL each) to remove unreacted compounds and byproducts.

### Fabrication of SWCNT Network Field-Effect Transistors

FETs were fabricated on glass substrates (Schott AF32eco, 300 μm thickness) that were passivated with the cross-linked polymer divinyltetramethylsiloxane-bis-benzocyclobutene (BCB).[35] Glass substrates were cleaned by ultrasonication in acetone and 2-propanol (10 min each). In a nitrogen-filled glovebox, a resin of BCB (Cyclotene 3022-35) was diluted with mesitylene, spin-coated onto the substrates (500 rpm for 3 s and then 8000 rpm for 60 s), and cross-linked via thermal annealing at 290 °C for 2 min. On these substrates, interdigitated bottom-contact electrodes (channel length $L$ = 20 μm and channel width $W$ = 10 mm) were patterned by photolithography (double-layer LOR5B/S1813 photoresist) and electron beam evaporation of chromium (3 nm) and gold (30 nm). After lift-off in *N*-methyl-2-pyrrolidone (NMP) overnight and rinsing with acetone and 2-propanol, the SWCNT networks were deposited onto the substrates, as detailed below. All SWCNT networks were annealed in an inert atmosphere at 150 °C for 45 min. Then, a double-layer gate dielectric was deposited, which consisted of a ∼10−14 nm poly(methyl methacrylate) (PMMA) layer and ∼60−65 nm hafnium oxide ($HfO_x$). First, a solution of PMMA (Polymer Source, $M_W$ = 315 kg $mol^{-1}$, syndiotactic) in *n*-butylacetate (6 g $L^{-1}$) was spin-coated at 4000 rpm for 60 s, followed by annealing at 80 °C for 2 min. Then, atomic layer deposition (Ultratech Savannah S100, 500 cycles, 100



https://doi.org/10.1021/acsaom.3c00261
ACS Appl. Opt. Mater. 2023, 1, 1706−1714

°C) was used to deposit the $HfO_x$ layer from a tetrakis-(dimethylamino)hafnium precursor (Strem Chemicals) with water as the oxidizing agent. To complete the devices, silver top-gate electrodes (30 nm) were thermally evaporated through a shadow mask.

### Deposition of SWCNT Networks

Concentrated dispersions of pristine and $sp^3$-functionalized (6,5) SWCNTs were obtained by bath sonication of SWCNT filter cakes in a small volume of fresh toluene with 1,10-phenanthroline (2.8 mmol $L^{-1}$) as the stabilizer.[49] From such dispersions with an optical density of 8 $cm^{-1}$ at the $E_{11}$ absorption transition, SWCNT networks were created by repeated spin-coating (2000 rpm, 30 s, 3 times) onto the prepatterned bottom-contact electrodes with intermediate annealing steps (100 °C, 2 min). Subsequently, substrates were rinsed with THF and 2-propanol. To remove all nanotubes outside the channel area, photolithography was performed as described above, followed by oxygen plasma treatment and lift-off in NMP for 60 min. Pristine and $sp^3$-functionalized (7,5) SWCNT networks were deposited via aerosol-jet printing (Optomec AJ200 printer, 200 $\mu$m inner diameter nozzle).[50] Terpineol (Sigma-Aldrich, mixture of isomers) was added (2 vol %) to SWCNT dispersions in toluene (optical density of 1−2 $cm^{-1}$ at the $E_{11}$ absorption transition) obtained by bath sonication of filter cakes to increase the viscosity and improve aerosol formation. The ink was printed exclusively in the channel area of the devices, which eliminated the need for patterning of the networks. During the printing process, the ink was constantly sonicated, and the substrates were placed on a heated stage at 100 °C. Finally, the substrates were rinsed with THF and 2-propanol to remove any residual polymer and terpineol.

### Spectroscopic Characterization

PL spectra of SWCNT dispersions and thin films were measured with a home-built setup. Samples were excited either with the wavelength-filtered output of a picosecond-pulsed supercontinuum laser (NKT Photonics SuperK Extreme, 19.5 MHz repetition rate) or with a 785 nm laser diode (Alphalas Picopower-LD-785-50) in continuous wave mode. The laser beam was focused on the sample (SWCNT dispersion in a quartz glass cuvette or SWCNT network FETs on transparent glass substrates) with a NIR-optimized 50× objective (Olympus, N.A. 0.65). Emitted photons were collected with the same objective, and scattered laser light was blocked by appropriate long-pass filters. The emission was spectrally resolved with a grating spectrograph (Acton SpectraPro SP2358, grating blaze 1200 nm, 150 lines $mm^{-1}$) and detected with a liquid nitrogen-cooled InGaAs line camera (Princeton Instruments OMA V:1024-1.7 LN). For time-resolved PL measurements in a time-correlated single-photon counting scheme, the spectrally selected emission was focused onto a gated InGaAs/InP avalanche photodiode (Micro Photon Devices) with a 20× objective (Mitutoyo, N.A. 0.40). Histograms of photon arrival times were recorded with a counting module (PicoQuant PicoHarp 300) and fitted with biexponential functions in a reconvolution procedure using SymPhoTime64 software. The instrument-limited decay of $E_{11}$ excitons in a dense (6,5) SWCNT film served as the instrument response function. For EL and PL spectroscopy at a constant gate voltage, SWCNT network FETs were electrically contacted and voltages were applied with a Keithley 2612A source meter. EL spectra were always recorded from the center of the channel to avoid possible effects of contact resistance or impact excitation at the electrode edges. All spectra were corrected to account for the absorption of optics in the detection path and the wavelength-dependent detector efficiency.

### Additional Characterization Techniques

Baseline-corrected absorption spectra of SWCNT dispersions were acquired with a Varian Cary 6000i UV−vis NIR spectrometer using quartz glass cuvettes with 1 cm path length. Raman spectra (532 and 633 nm excitation) were measured with a Renishaw inVia Reflex confocal Raman microscope with a 50× objective (N.A. 0.50) in the backscattering configuration. Typically, Raman data were obtained by averaging over 2500 individual spectra collected from an area of 100 × 100 $\mu m^2$. Atomic force micrographs of SWCNT networks were recorded with a Bruker Dimension Icon atomic force microscope in the ScanAsyst mode. Thicknesses of the polymer and $HfO_x$ films were determined with a Bruker DektakXT Stylus profilometer. The current−voltage characteristics of SWCNT network FETs were recorded with an Agilent 4156C semiconductor parameter analyzer. Effective device capacitances were extracted from capacitance versus gate voltage sweeps with a Solatron Analytical ModuLab XM MTS impedance analyzer at a frequency of 100 Hz. They varied between 130 and 137 nF $cm^{-2}$ for (6,5) SWCNT network FETs and between 87 and 88 nF $cm^{-2}$ for the (7,5) SWCNT network FETs.

## ■ ASSOCIATED CONTENT

### Supporting Information

The Supporting Information is available free of charge at https://pubs.acs.org/doi/10.1021/acsaom.3c00261.

> Absorption and Raman spectra of pristine and functionalized (6,5) and (7,5) SWCNTs, analysis of the gate voltage-dependent PL quenching of SWCNT networks, time-resolved PL spectroscopy and extracted PL lifetimes depending on gating, and electroluminescence spectra from pristine SWCNT networks (PDF)

## ■ AUTHOR INFORMATION


### Corresponding Author

**Jana Zaumseil** − *Institute for Physical Chemistry, Universität Heidelberg, D-69120 Heidelberg, Germany;* orcid.org/0000-0002-2048-217X; Email: zaumseil@uni-heidelberg.de

### Authors

**Nicolas F. Zorn** − *Institute for Physical Chemistry, Universität Heidelberg, D-69120 Heidelberg, Germany;* orcid.org/0000-0001-9651-5612

**Simon Settele** − *Institute for Physical Chemistry, Universität Heidelberg, D-69120 Heidelberg, Germany;* orcid.org/0000-0002-0082-2587

**Finn L. Sebastian** − *Institute for Physical Chemistry, Universität Heidelberg, D-69120 Heidelberg, Germany;* orcid.org/0000-0003-1161-633X

**Sebastian Lindenthal** − *Institute for Physical Chemistry, Universität Heidelberg, D-69120 Heidelberg, Germany*

Complete contact information is available at: https://pubs.acs.org/10.1021/acsaom.3c00261


### Author Contributions

N.F.Z. fabricated and measured all samples and analyzed the data. S.S. and F.L.S. fabricated selected samples, contributed to characterization, and prepared chemically functionalized SWCNT dispersions. S.L. prepared (7,5) SWCNT dispersions. J.Z. conceived and supervised the project. N.F.Z. and J.Z. wrote the manuscript with input from all authors.

### Notes

The authors declare no competing financial interest.

## ■ ACKNOWLEDGMENTS

This project has received funding from the European Research Council (ERC) under the European Union's Horizon 2020 research and innovation programme (Grant Agreement No. 817494 "TRIFECTs").

## REFERENCES


(1) Li, C.; Wang, Q. Challenges and Opportunities for Intravital near-Infrared Fluorescence Imaging Technology in the Second Transparency Window. *ACS Nano* **2018**, *12*, 9654−9659.
(2) Hong, G.; Antaris, A. L.; Dai, H. Near-Infrared Fluorophores for Biomedical Imaging. *Nat. Biomed. Eng.* **2017**, *1*, 0010.
(3) Biniek, L.; Schroeder, B. C.; Nielsen, C. B.; McCulloch, I. Recent Advances in High Mobility Donor-Acceptor Semiconducting Polymers. *J. Mater. Chem.* **2012**, *22*, 14803−14813.
(4) Zampetti, A.; Minotto, A.; Cacialli, F. Near-Infrared (NIR) Organic Light-Emitting Diodes (Oleds): Challenges and Opportunities. *Adv. Funct. Mater.* **2019**, *29*, 1807623.
(5) Held, M.; Zakharko, Y.; Wang, M.; Jakubka, F.; Gannott, F.; Rumer, J. W.; Ashraf, R. S.; McCulloch, I.; Zaumseil, J. Photo- and Electroluminescence of Ambipolar, High-Mobility, Donor-Acceptor Polymers. *Org. Electr.* **2016**, *32*, 220−227.
(6) Steckler, T. T.; Lee, M. J.; Chen, Z.; Fenwick, O.; Andersson, M. R.; Cacialli, F.; Sirringhaus, H. Multifunctional Materials for OFETs, LEFETs and NIR PLEDs. *J. Mater. Chem. C* **2014**, *2*, 5133−5141.
(7) Englman, R.; Jortner, J. The Energy Gap Law for Radiationless Transitions in Large Molecules. *Mol. Phys.* **1970**, *18*, 145−164.
(8) Jiao, M.; Portniagin, A. S.; Luo, X.; Jing, L.; Han, B.; Rogach, A. L. Semiconductor Nanocrystals Emitting in the Second near-Infrared Window: Optical Properties and Application in Biomedical Imaging. *Adv. Opt. Mater.* **2022**, *10*, 2200226.
(9) Gong, X.; Yang, Z.; Walters, G.; Comin, R.; Ning, Z.; Beauregard, E.; Adinolfi, V.; Voznyy, O.; Sargent, E. H. Highly Efficient Quantum Dot near-Infrared Light-Emitting Diodes. *Nat. Photonics* **2016**, *10*, 253−257.
(10) Wang, L.; Zhao, Z.; Wei, C.; Wei, H.; Liu, Z.; Bian, Z.; Huang, C. Review on the Electroluminescence Study of Lanthanide Complexes. *Adv. Opt. Mater.* **2019**, *7*, 1801256.
(11) Avouris, P.; Freitag, M.; Perebeinos, V. Carbon-Nanotube Photonics and Optoelectronics. *Nat. Photonics* **2008**, *2*, 341−350.
(12) Wei, X.; Li, S.; Wang, W.; Zhang, X.; Zhou, W.; Xie, S.; Liu, H. Recent Advances in Structure Separation of Single-Wall Carbon Nanotubes and Their Application in Optics, Electronics, and Optoelectronics. *Adv. Sci.* **2022**, *9*, 2200054.
(13) Berger, F. J.; Higgins, T. M.; Rother, M.; Graf, A.; Zakharko, Y.; Allard, S.; Matthiesen, M.; Gotthardt, J. M.; Scherf, U.; Zaumseil, J. From Broadband to Electrochromic Notch Filters with Printed Monochiral Carbon Nanotubes. *ACS Appl. Mater. Interfaces* **2018**, *10*, 11135−11142.
(14) Graf, A.; Murawski, C.; Zakharko, Y.; Zaumseil, J.; Gather, M. C. Infrared Organic Light-Emitting Diodes with Carbon Nanotube Emitters. *Adv. Mater.* **2018**, *30*, 1706711.
(15) Jakubka, F.; Grimm, S. B.; Zakharko, Y.; Gannott, F.; Zaumseil, J. Trion Electroluminescence from Semiconducting Carbon Nanotubes. *ACS Nano* **2014**, *8*, 8477−8486.
(16) Graf, A.; Held, M.; Zakharko, Y.; Tropf, L.; Gather, M. C.; Zaumseil, J. Electrical Pumping and Tuning of Exciton-Polaritons in Carbon Nanotube Microcavities. *Nat. Mater.* **2017**, *16*, 911−917.
(17) Graf, A.; Zakharko, Y.; Schießl, S. P.; Backes, C.; Pfohl, M.; Flavel, B. S.; Zaumseil, J. Large Scale, Selective Dispersion of Long Single-Walled Carbon Nanotubes with High Photoluminescence Quantum Yield by Shear Force Mixing. *Carbon* **2016**, *105*, 593−599.
(18) Steiner, M.; Freitag, M.; Perebeinos, V.; Naumov, A.; Small, J. P.; Bol, A. A.; Avouris, P. Gate-Variable Light Absorption and Emission in a Semiconducting Carbon Nanotube. *Nano Lett.* **2009**, *9*, 3477−3481.
(19) Hertel, T.; Himmelein, S.; Ackermann, T.; Stich, D.; Crochet, J. Diffusion Limited Photoluminescence Quantum Yields in 1-D Semiconductors: Single-Wall Carbon Nanotubes. *ACS Nano* **2010**, *4*, 7161−7168.
(20) Ghosh, S.; Bachilo, S. M.; Simonette, R. A.; Beckingham, K. M.; Weisman, R. B. Oxygen Doping Modifies Near-Infrared Band Gaps in Fluorescent Single-Walled Carbon Nanotubes. *Science* **2010**, *330*, 1656−1659.
(21) Piao, Y.; Meany, B.; Powell, L. R.; Valley, N.; Kwon, H.; Schatz, G. C.; Wang, Y. Brightening of Carbon Nanotube Photoluminescence through the Incorporation of $sp^3$ Defects. *Nat. Chem.* **2013**, *5*, 840−845.
(22) Gifford, B. J.; Kilina, S.; Htoon, H.; Doorn, S. K.; Tretiak, S. Exciton Localization and Optical Emission in Aryl-Functionalized Carbon Nanotubes. *J. Phys. Chem. C* **2018**, *122*, 1828−1838.
(23) Danné, N.; Kim, M.; Godin, A. G.; Kwon, H.; Gao, Z.; Wu, X.; Hartmann, N. F.; Doorn, S. K.; Lounis, B.; Wang, Y.; Cognet, L. Ultrashort Carbon Nanotubes That Fluoresce Brightly in the near-Infrared. *ACS Nano* **2018**, *12*, 6059−6065.
(24) Brozena, A. H.; Kim, M.; Powell, L. R.; Wang, Y. Controlling the Optical Properties of Carbon Nanotubes with Organic Colour-Centre Quantum Defects. *Nat. Rev. Chem.* **2019**, *3*, 375−392.
(25) Settele, S.; Berger, F. J.; Lindenthal, S.; Zhao, S.; El Yumin, A. A.; Zorn, N. F.; Asyuda, A.; Zharnikov, M.; Högele, A.; Zaumseil, J. Synthetic Control over the Binding Configuration of Luminescent $sp^3$-Defects in Single-Walled Carbon Nanotubes. *Nat. Commun.* **2021**, *12*, 2119.
(26) Zaumseil, J. Luminescent Defects in Single-Walled Carbon Nanotubes for Applications. *Adv. Opt. Mater.* **2022**, *10*, 2101576.
(27) Sebastian, F. L.; Zorn, N. F.; Settele, S.; Lindenthal, S.; Berger, F. J.; Bendel, C.; Li, H.; Flavel, B. S.; Zaumseil, J. Absolute Quantification of $sp^3$ Defects in Semiconducting Single-Wall Carbon Nanotubes by Raman Spectroscopy. *J. Phys. Chem. Lett.* **2022**, *13*, 3542−3548.
(28) Berger, F. J.; Lüttgens, J.; Nowack, T.; Kutsch, T.; Lindenthal, S.; Kistner, L.; Müller, C. C.; Bongartz, L. M.; Lumsargis, V. A.; Zakharko, Y.; Zaumseil, J. Brightening of Long, Polymer-Wrapped Carbon Nanotubes by $sp^3$ Functionalization in Organic Solvents. *ACS Nano* **2019**, *13*, 9259−9269.
(29) He, X.; Hartmann, N. F.; Ma, X.; Kim, Y.; Ihly, R.; Blackburn, J. L.; Gao, W.; Kono, J.; Yomogida, Y.; Hirano, A.; Tanaka, T.; Kataura, H.; Htoon, H.; Doorn, S. K. Tunable Room-Temperature Single-Photon Emission at Telecom Wavelengths from $sp^3$ Defects in Carbon Nanotubes. *Nat. Photonics* **2017**, *11*, 577.
(30) Wang, P.; Fortner, J.; Luo, H.; Kłos, J.; Wu, X.; Qu, H.; Chen, F.; Li, Y.; Wang, Y. Quantum Defects: What Pairs with the Aryl Group When Bonding to the $sp^2$ Carbon Lattice of Single-Wall Carbon Nanotubes? *J. Am. Chem. Soc.* **2022**, *144*, 13234−13241.
(31) Li, M.-K.; Riaz, A.; Wederhake, M.; Fink, K.; Saha, A.; Dehm, S.; He, X.; Schöppler, F.; Kappes, M. M.; Htoon, H.; Popov, V. N.; Doorn, S. K.; Hertel, T.; Hennrich, F.; Krupke, R. Electroluminescence from Single-Walled Carbon Nanotubes with Quantum Defects. *ACS Nano* **2022**, *16*, 11742−11754.
(32) Xu, B.; Wu, X.; Kim, M.; Wang, P.; Wang, Y. Electroluminescence from 4-Nitroaryl Organic Color Centers in Semiconducting Single-Wall Carbon Nanotubes. *J. Appl. Phys.* **2021**, *129*, 044305.
(33) Zorn, N. F.; Berger, F. J.; Zaumseil, J. Charge Transport in and Electroluminescence from $sp^3$-Functionalized Carbon Nanotube Networks. *ACS Nano* **2021**, *15*, 10451−10463.
(34) Yu, B.; Naka, S.; Aoki, H.; Kato, K.; Yamashita, D.; Fujii, S.; Kato, Y. K.; Fujigaya, T.; Shiraki, T. Ortho-Substituted Aryldiazonium Design for the Defect Configuration-Controlled Photoluminescent Functionalization of Chiral Single-Walled Carbon Nanotubes. *ACS Nano* **2022**, *16*, 21452−21461.
(35) Zorn, N. F.; Settele, S.; Zhao, S.; Lindenthal, S.; El Yumin, A. A.; Wedl, T.; Li, H.; Flavel, B. S.; Högele, A.; Zaumseil, J. Near-Intrinsic Photo- and Electroluminescence from Single-Walled Carbon Nanotube Thin Films on BCB-Passivated Surfaces. *Adv. Opt. Mater.* **2023**, *11*, 2300236.
(36) Schießl, S. P.; Rother, M.; Lüttgens, J.; Zaumseil, J. Extracting the Field-Effect Mobilities of Random Semiconducting Single-Walled Carbon Nanotube Networks: A Critical Comparison of Methods. *Appl. Phys. Lett.* **2017**, *111*, 193301.
(37) Rother, M.; Schießl, S. P.; Zakharko, Y.; Gannott, F.; Zaumseil, J. Understanding Charge Transport in Mixed Networks of Semi-



https://doi.org/10.1021/acsaom.3c00261
ACS Appl. Opt. Mater. 2023, 1, 1706−1714

conducting Carbon Nanotubes. *ACS Appl. Mater. Interfaces* **2016**, *8*, 5571−5579.
(38) Zheng, W.; Zorn, N. F.; Bonn, M.; Zaumseil, J.; Wang, H. I. Probing Carrier Dynamics in $sp^3$-Functionalized Single-Walled Carbon Nanotubes with Time-Resolved Terahertz Spectroscopy. *ACS Nano* **2022**, *16*, 9401−9409.
(39) Freitag, M.; Steiner, M.; Naumov, A.; Small, J. P.; Bol, A. A.; Perebeinos, V.; Avouris, P. Carbon Nanotube Photo- and Electroluminescence in Longitudinal Electric Fields. *ACS Nano* **2009**, *3*, 3744−3748.
(40) Yoshida, M.; Popert, A.; Kato, Y. K. Gate-Voltage Induced Trions in Suspended Carbon Nanotubes. *Phys. Rev. B* **2016**, *93*, 041402.
(41) Zorn, N. F.; Scuratti, F.; Berger, F. J.; Perinot, A.; Heimfarth, D.; Caironi, M.; Zaumseil, J. Probing Mobile Charge Carriers in Semiconducting Carbon Nanotube Networks by Charge Modulation Spectroscopy. *ACS Nano* **2020**, *14*, 2412−2423.
(42) Tanaka, Y.; Hirana, Y.; Niidome, Y.; Kato, K.; Saito, S.; Nakashima, N. Experimentally Determined Redox Potentials of Individual (n,m) Single-Walled Carbon Nanotubes. *Angew. Chem., Int. Ed.* **2009**, *48*, 7655−7659.
(43) Shiraishi, T.; Juhász, G.; Shiraki, T.; Akizuki, N.; Miyauchi, Y.; Matsuda, K.; Nakashima, N. Determination of Precise Redox Properties of Oxygen-Doped Single-Walled Carbon Nanotubes Based on in Situ Photoluminescence Electrochemistry. *J. Phys. Chem. C* **2016**, *120*, 15632−15639.
(44) Shiraishi, T.; Shiraki, T.; Nakashima, N. Substituent Effects on the Redox States of Locally Functionalized Single-Walled Carbon Nanotubes Revealed by in Situ Photoluminescence Spectroelectrochemistry. *Nanoscale* **2017**, *9*, 16900−16907.
(45) Kim, M.; Wu, X.; Ao, G.; He, X.; Kwon, H.; Hartmann, N. F.; Zheng, M.; Doorn, S. K.; Wang, Y. Mapping Structure-Property Relationships of Organic Color Centers. *Chem.* **2018**, *4*, 2180−2191.
(46) Hartmann, N. F.; Velizhanin, K. A.; Haroz, E. H.; Kim, M.; Ma, X.; Wang, Y.; Htoon, H.; Doorn, S. K. Photoluminescence Dynamics of Aryl $sp^3$ Defect States in Single-Walled Carbon Nanotubes. *ACS Nano* **2016**, *10*, 8355−8365.
(47) He, X.; Velizhanin, K. A.; Bullard, G.; Bai, Y.; Olivier, J.-H.; Hartmann, N. F.; Gifford, B. J.; Kilina, S.; Tretiak, S.; Htoon, H.; Therien, M. J.; Doorn, S. K. Solvent- and Wavelength-Dependent Photoluminescence Relaxation Dynamics of Carbon Nanotube $sp^3$ Defect States. *ACS Nano* **2018**, *12*, 8060−8070.
(48) Zaumseil, J. Recent Developments and Novel Applications of Thin Film, Light-Emitting Transistors. *Adv. Funct. Mater.* **2020**, *30*, 1905269.
(49) Schneider, S.; Lefebvre, J.; Diercks, N. J.; Berger, F. J.; Lapointe, F.; Schleicher, J.; Malenfant, P. R. L.; Zaumseil, J. Phenanthroline Additives for Enhanced Semiconducting Carbon Nanotube Dispersion Stability and Transistor Performance. *ACS Appl. Nano Mater.* **2020**, *3*, 12314−12324.
(50) Rother, M.; Brohmann, M.; Yang, S.; Grimm, S. B.; Schießl, S. P.; Graf, A.; Zaumseil, J. Aerosol-Jet Printing of Polymer-Sorted (6,5) Carbon Nanotubes for Field-Effect Transistors with High Reproducibility. *Adv. Electron. Mater.* **2017**, *3*, 1700080.


https://doi.org/10.1021/acsaom.3c00261
*ACS Appl. Opt. Mater.* 2023, 1, 1706−1714